Charge-density analysis and electrostatic properties of 2-carboxy-4-methylanilinium chloride monohydrate obtained using a multipolar and a spherical-charges model

Noureddine Dadda, Ayoub Nassour, Benoit Guillot, Nourredine Benali-Cherif, Christian Jelsch

Acta Crystallographica Section A
Foundations of Crystallography
ISSN 0108-7673

Received 24 February 2012
Accepted 16 April 2012

Charge-density analysis and electrostatic properties of 2-carboxy-4-methylanilinium chloride monohydrate obtained using a multipolar and a spherical-charges model

Noureddine Dadda,[a,b] Ayoub Nassour,[a] Benoît Guillot,[a] Nourredine Benali-Cherif[b] and Christian Jelsch[a]*

[a]Laboratoire de Cristallographie, Résonance Magnétique et Modélisations (CRM2), CNRS, UMR 7036, Institut Jean Barriol, Faculté des Sciences et Technologies, Université de Lorraine, BP 70239, 54506 Vandoeuvre-lès-Nancy Cedex, France, and [b]Laboratoire des Structures, Propriétés et Interactions Inter Atomique (LASPI2A), Université Abbes Laghrour-Khenchela 40000, Algeria. Correspondence e-mail: christian.jelsch@crm2.uhp-nancy.fr

The new crystal structure of 2-carboxy-4-methylanilinium chloride monohydrate was determined by X-ray diffraction and refined using three different electron-density models. In the first model, the ELMAM2 multipolar electron-density database was transferred to the molecule. Theoretical structure factors were also computed from periodic density functional theory calculations and yielded, after multipolar-atoms refinement, the second charge-density model. An alternative electron-density modelling, based on spherical atoms and additional charges on the covalent bonds and electron lone-pair sites, was used in the third model in the refinement *versus* the theoretical data. The crystallographic refinements, structural properties, electron-density distributions and molecular electrostatic potentials obtained from the different charge-density models were compared. As the number of variables refined in the different models is the same, the *R* factor is a good indicator of refinement quality. The *R* factor is best for multipolar modelling, presumably because of the greater flexibility and larger number of parameters to model the electron density compared to the spherical-charges model. The electrostatic potentials around the molecule show a high correlation coefficient between the three models.

1. Introduction

The compound 2-carboxy-4-methylaniline [or 2-amino-5-methylbenzoic acid, (I)] is a biologically active molecule which serves as a pharmaceutical intermediate (Zheng *et al.*, 2007). From (I), a variety of derivatives have been synthesized which might be potential agents for anti-cancer chemotherapy (Cao *et al.*, 2005, 2006, 2009). The substance (CAS Number: 2341-78-8) irritates the eyes and the skin, and may cause respiratory irritation as well.

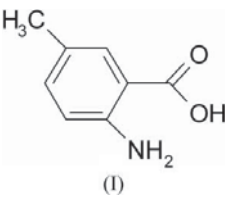

(I)

The title compound (CMA) is the monohydrated chloride salt of (I) (Table 1). Its crystal structure with thermal ellipsoids is shown in Fig. 1. It was determined as part of investigations into the structural characteristics of organic–inorganic layered compounds and an ongoing study of D—H$\cdots A$ hydrogen bonding in hybrid material systems.

Here, the charge density of CMA was derived by several methods (see Table 2), including periodic quantum-mechanics calculations. Databanks describing the atomic electron density allow crystal structure refinements using transferred aspherical scattering factors. Such charge-density transfer has been shown in the literature to be advantageous compared to the independent-atom model (IAM). Compared to the conventional spherical-atom refinement, the crystallographic statistics are improved and anisotropic thermal displacement parameters are deconvoluted from (*i.e.* do not incorporate) the bonding electron density.

The transferability principle was applied to build a charge-density model of the title compound and to compare this model with the electron density refined against theoretical structure factors. The principle of transferability of electron-density parameters was first applied in the early 1990s by Brock *et al.* (1991). It is based on the hypothesis that the electron-density deformation features are similar, at first approximation, for a given atomic type in different molecules

Table 1
Crystal and data-collection experimental details.

Empirical formula	HOOC–C_7H_6–NH_3^+·Cl^-·H_2O
Formula weight (g mol^{-1})	205.631
Space group	$P2_1/c$
Unit cell (Å, °)	a = 10.051 (4)
	b = 4.963 (2)
	c = 19.563 (15)
	β = 96.77 (2)
V (Å^3), Z	969.0 (9), 4
Crystal shape	Prism
Crystal size (mm)	0.24 × 0.19 × 0.13
Colour	Yellow
Radiation type	Mo $K\alpha$
Temperature (K)	100 (2)
Wavelength (Å)	0.71073
hkl(min)	−13, −5, −26
hkl(max)	14, 7, 26
R_{int}	0.055
Redundancy	4.3
Absorption T_{min}/T_{max}	0.9298/0.9711
Weighting scheme	$1/[\sigma^2(F_o^2) + (0.1P)^2 + 0.01P]$, $P = (2F_o^2 + F_c^2)/3$

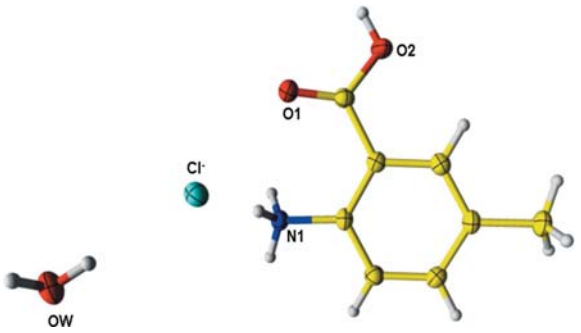

Figure 1
View of 2-carboxy-4-methylanilinium chloride monohydrate at 100 K. The thermal ellipsoids are shown with 60% probability and the diagram was generated with *MoProViewer* (Guillot, 2011).

or in different crystals. The charge-density distribution can thus be transferred onto a crystal structure without any further multipolar refinement.

Therefore, as a result of various research studies, several libraries of transferable charge-density parameters, either experimental (Pichon-Pesme *et al.*, 1995; Domagała *et al.*, 2011) or theoretical (Dittrich *et al.*, 2005; Volkov *et al.*, 2004), were developed. The advantages of using aspherical-atom databases in routine crystallographic modelling were pointed out in several studies (Jelsch *et al.*, 1998, 2005; Dittrich *et al.*, 2007, 2008; Dittrich, Hübschle *et al.*, 2006, 2009; Dittrich, Strumpel *et al.*, 2006; Dittrich, Weber *et al.*, 2009; Zarychta *et al.*, 2007; Bąk *et al.*, 2009). The ELMAM library, developed in our laboratory, is based on averaging multipolar parameters obtained from experimental charge-density analyses of peptides and amino acids; it enables one to model the electron density in protein structures (Pichon-Pesme *et al.*, 2004; Zarychta *et al.*, 2007). The database was extended to ELMAM2 (Domagała *et al.*, 2011), which is adapted to common organic molecules and is now based on optimal local coordinate systems (Domagała & Jelsch, 2008). New chemical environments (atom types) can be easily added to the database when new charge-density diffraction data become publicly available. In this work, the application of the extended ELMAM2 database for the multipolar-atom modelling of compound CMA (Fig. 1) is presented. The most important features of the modelled electron density of this compound are discussed and are subject to a detailed comparison with the theoretical 'multipole' model refined against structure factors obtained from periodic quantum-mechanical calculations (Dovesi *et al.*, 2010).

Furthermore, a model based on dummy bond charge (virtual-atoms modelling) was refined against the theoretical structure factors. This approach allows the modelling of the electron density as an alternative to the classical Hansen & Coppens (1978) multipolar-atom model. Such spherical-charges modelling has already been applied in a few cases in the literature: it was reported for urea (Scheringer, Kutoglu *et al.*, 1978; Scheringer, Mullen, Hellner, Hase *et al.*, 1978; Mullen & Hellner, 1978*a*), thiourea (Scheringer, Kutoglu *et al.*, 1978; Scheringer, Mullen, Hellner, Hase *et al.*, 1978; Mullen & Hellner, 1978*b*), diborane (Mullen & Hellner, 1977; Scheringer, Mullen & Hellner, 1978), decaborane (Dietrich *et al.*, 1979), cyanuric acid (Dietrich *et al.*, 1979) and silicon (Scheringer, 1980). More recently, the modelling of bond scatterers was applied by Afonine *et al.* (2004, 2007) in the refinement of proteins at ultra-high resolution.

Improvements of the residual electron density and crystallographic R factors upon electron-density transfer are thoroughly discussed for the three different modelling approaches. The charge-density features and the derived molecular electrostatic potential and interaction energies are analysed.

Table 2
Summary of the electron-density models and crystallographic refinements.

SCA, *XYZ*, *UIJ* refer to scale factor, atomic coordinates and thermal displacement parameters, respectively. H and *Q* refer to hydrogen and virtual atoms, respectively. Diffraction data are obtained by theoretical calculations (THEO) or experimentally (EXP).

Model name	Refinement	*hkl* data	Restraints and constraints
THEO_MUL	Geometry fixed. P_{val}, P_{lm}, κ, κ' refined	THEO	κ of H atoms restrained. Chemical equivalence of H atoms
THEO_VIR	Geometry fixed. *XYZ* of *Q* atoms, P_{val} and κ of all atoms refined	THEO	κ of H atoms restrained. Stereochemical restraints for *Q*. Chemical equivalence of H and *Q*
EXP_IAM	*SCA XYZ UIJ* refined except for H atoms	EXP	Stereochemical and thermal constraints on H atoms
EXP_ELMAM2	*SCA XYZ UIJ* refined except for H atoms	EXP	Stereochemical and thermal constraints on H atoms
EXP_MUL	*SCA XYZ UIJ* refined except for H atoms	EXP	Stereochemical and thermal constraints on H atoms
EXP_VIR	*SCA XYZ UIJ* refined except for H and *Q* atoms	EXP	Stereochemical constraints on H. Thermal constraints on H and *Q*

2. Experimental and theoretical details

2.1. Crystallization

Compound (I) was purchased from Aldrich and is presented as a light-yellow powder. Single crystals of the title compound (CMA), HOOC–C_7H_6–NH_3^+·Cl^-·H_2O, were obtained by re-crystallizing compound (I) in an aqueous solution of hydrochloric acid (1 *M*). Concentrated hydrochloric acid was slowly added to the aqueous solution and compound (I) was dissolved by stirring and slow heating. The resulting saturated aqueous solution was kept at room temperature to evaporate slowly. Yellow crystals started appearing after a week.

2.2. Data collection

A yellow prism-shaped crystal with dimensions 0.24 × 0.19 × 0.13 mm was used for 100 K data collection performed using a Kappa CCD APEXII diffractometer. Reflections were collected using Mo radiation (λ = 0.71073 Å) and a graphite monochromator. The diffraction data were measured on the CCD detector, ranging from 4.09 to 28.2° in the θ position. The exposure time for each frame was set to 10 s. A standard scan width of 1° in ω was chosen for this experiment in order to reconstruct the intensity peak profiles. A total of 2276 unique reflections were obtained up to a reciprocal resolution of $\sin\theta/\lambda = 0.663$ Å^{-1} and used in the refinements. The details and the statistics on the X-ray diffraction data are listed in Table 1. The diffraction data were averaged (scaled and merged) with the program *SORTAV* (Blessing, 1997). The space group was determined to be monoclinic $P2_1/c$ with $Z = 4$.

2.3. Spherical-atom model refinement

Structure solution and the initial stages of refinement were carried out using *SHELX97* (Sheldrick, 2008) with full-matrix least squares and based on diffraction intensities. The final refinements were performed on structure-factor amplitudes using the *MoPro* package (Guillot *et al.*, 2001; Jelsch *et al.*, 2005). In this first refinement, the chloride monohydrate of 2-carboxy-4-methylanilinium was modelled using the IAM approximation. Scale factor, atomic positions and anisotropic displacement parameters (ADPs) for all heavy atoms were refined until convergence. The H-atom parameters were not refined but constrained: H—*X* distances were set to standard X-ray diffraction distances, similarly to the *SHELXL* program (Sheldrick, 2008). Isotropic thermal parameters of H atoms U_{eq} were riding on the U_{eq} of the bonded atom with a multiplying factor of 1.5, except for the H—C atoms on the aromatic ring for which a factor 1.2 was applied.

2.4. Theoretical structure factors

Density functional theory (DFT) B3LYP periodic theoretical calculation was performed using the program *CRYSTAL09* (Dovesi *et al.*, 2010). The crystal structure obtained from the X-ray diffraction experiment was used as the starting geometry, optimization was performed with DFT (Hohenberg & Kohn, 1964) and with the B3LYP hybrid functional (Lee *et al.*, 1988) using the 6-31G(d,p) basis set (Hariharan & Pople, 1973). The level of accuracy in evaluating the Coulomb and exchange series is controlled by five parameters, for which values of 10^{-6}, 10^{-6}, 10^{-6}, 10^{-6} and 10^{-17} were used for the Coulomb and the exchange series. The shrinking factor of the reciprocal space was set to 4, corresponding to 30 *k* points in the irreducible Brillouin zone in which the Hamiltonian matrix was diagonalized. Upon energy convergence (10^{-8} hartree), the periodic wavefunction based on the optimized geometry was obtained. The coordinates of the H atoms were relaxed (optimized), but the unit-cell dimensions were kept fixed. The option XFAC was used to generate a unique set of 15 843 theoretical structure factors (up to $\sin\theta/\lambda = 1.25$ A^{-1} reciprocal resolution) from the computed electron density.

2.5. Multipolar theoretical refinement

Multipolar refinements were performed using the Hansen–Coppens model (Hansen & Coppens, 1978) implemented in the *MoPro* package (Guillot *et al.*, 2001; Jelsch *et al.*, 2005). The aspherical-atom electron density is modelled by

$$\rho_{\rm atom}(r) = \rho_{\rm core}(r) + P_{\rm val}\kappa^3\rho_{\rm val}(\kappa r) + \sum_{l=0}^{l_{\rm max}} \kappa'^3 R_l(\kappa' r) \sum_{m=0}^{l} P_{lm\pm} y_{lm\pm}(\theta, \varphi). \quad (1)$$

The first two terms represent the core $\rho_{\rm core}$ and the valence electrons $\rho_{\rm val}$ of the atom while the third term is a sum of angular functions ($y_{lm\pm}$) describing the multipolar population. The angular functions $y_{lm\pm}$ are real spherical harmonic functions which are normalized for electron density. The coefficients $P_{\rm val}$ and $P_{lm\pm}$ are the populations of the spherical and multipolar valence electron density, respectively. κ and κ' are parameters enabling the expansion or contraction of the valence shell. The form factors of the core and valence electrons were calculated using the free-atom Clementi wavefunction (Clementi & Roetti, 1974). Multipoles were developed up to the hexadecapoles level for the Cl atom, while those of O and C were up to octupoles. For H atoms, one dipole and one quadrupole directed along the H—*X* axis were modelled. Refinements using the *MoPro* package (Jelsch *et al.*, 2005) were performed *versus* the theoretical structure-factor amplitudes F_{hkl} and *versus* experimental intensities I_{hkl}.

The multipolar-atom refinement for THEO_MUL (see Table 2) was done in the following manner. (i) The atomic positions were kept fixed to the values obtained from the relaxation geometry. (ii) The scale factor was fixed to the absolute value (1.0). (iii) The atomic thermal motion parameters were set to zero. (iv) Restraints or constraints on the electron-density distribution were imposed only on the H atoms. Their κ parameters were restrained to a value of 1.16 (1) (Stewart, 1976). Chemical equivalencies (Domagała *et al.*, 2011) were applied on the charge density of H atoms. (v) The valence and multipole populations, κ and κ' parameters were refined sequentially, until convergence. The charge density obtained from theoretical structure factors was refined until convergence.

The static and deformation maps were calculated using the *VMoPro* module of the *MoPro* software (Guillot *et al.*, 2001; Jelsch *et al.*, 2005) and the molecular view with thermal ellipsoids was produced with *MoProViewer* (Guillot, 2011).

2.6. Virtual-spherical-charges model

In small-molecule crystallography, the molecular distribution of electron density is generally approximated by the spherical-atom model (IAM). Obviously, this model is an approximation of the real electron density in molecules. Accurate electron density in the crystal can be derived from aspherical correction terms in the atomic model (Hirshfeld, 1971; Stewart, 1976). The 'multipolar' atom model, developed by Hansen & Coppens (1978), is now the most widely used in charge-density analysis. This model describes the electron density as a sum of pseudo-atomic densities composed of a spherical part and a 'multipolar' part. The atomic electron density obtained from the multipolar model deviates from the spherical model by an accumulation of electrons on the covalent bonds. For the O, N and Cl atoms, the electron lone-pair regions also show a significant electron accumulation. Based on these considerations, a new empirical model was developed in order to reproduce results of a quality comparable to that of the 'multipolar' model. The electron density is considered as a superposition of real and virtual spherical atoms:

$$\rho(r) = \sum_{\text{atom}} \rho_{\text{core}}(r) + P_{\text{val}}\kappa^3\rho_{\text{val}}(\kappa r) + \sum_{\text{vir}} P_{\text{vir}}\kappa_{\text{vir}}^3\rho_{\text{vir}}(\kappa r), \quad (2)$$

where ρ_{core} and ρ_{val} are the core and spherical valence electron densities that can be calculated from Hartree–Fock (HF) or DFT methods. The real atoms (C, O, N, Cl and H here) were treated spherically; these atoms can be described as the first and second terms of equation (2). The third term corresponds to the electron density ρ_{vir} generated by the virtual atoms. It shows some similarity with the second term of the Hansen & Coppens equation [see equation (1)]: the refined parameters are a spherical valence population P_{vir} and an expansion/contraction coefficient κ_{vir}. The atomic wavefunctions of Clementi & Roetti (1974), which are extensively used in X-ray charge-density refinement, were applied to the real atoms.

The same Slater-type wavefunction was adopted for the dummy bond charge (DBC) optimized by a least-squares method. The virtual density $\rho_{\text{vir}}(r)$ was fitted from a residual Fourier electron density calculated from the spherical-atom modelling with theoretical structure factors up to $\sin\theta/\lambda$ = 0.70 A^{-1} reciprocal resolution. A centrosymmetric crystal, DL-histidine (Coppens *et al.*, 1999), was selected and the theoretical structure factors were computed with the same methodology as described for CMA in this paper. The residual density was fitted in a d = [0., 1.] Å distance interval around the Cα—Cβ bonding density peak of the amino acid in the plane perpendicular to the Cα—Cβ bond to avoid effects of the real atoms on the density. As the residual density shows a parabolic shape in the area around the maximum, the $\rho_{\text{vir}}(r)$ function was imposed to have a zero derivative at the virtual-atom position (r = 0). The wavefunction coefficients and the orbital exponents for the virtual atom are given in the supplementary material[1] and the resulting $\rho_{\text{vir}}(r)$ curve is shown in Fig. 2. The Q_{AB} and Q_{LP} virtual atoms refer, in this paper, to the bonding density between atoms A and B and to the charge located on the expected oxygen electron lone-pair sites, respectively. The Q_{LP} lone pairs were assigned the same wavefunction description as the Q_{AB} atoms but, as they are more contracted in space, refined to larger κ values.

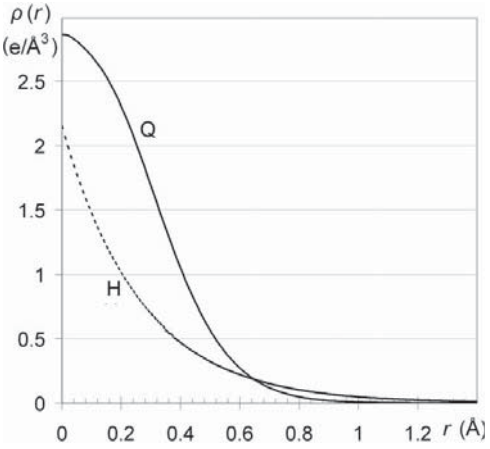

Figure 2
Electron density of a spherical virtual atom with P_{vir} = 1 as a function of the distance r to the nucleus. For comparison, the same curve is shown for an H atom.

2.7. Restraining the virtual atoms

The stereochemical restraints implemented in *MoPro* concern notably interatomic distances, distance similarity, linearity of A—Q_{AB}—B segments and planarity. The restraints use quadratic functions and minimize the squared difference between the actual and ideal values; the weight of the restraint is the square inverse of the restraint sigma value. The position of virtual charges had to be stabilized by stereochemical restraints or constraints. The bond virtual atoms' positions were refined and prevented from deviating from the bond line by using linearity constraints for A—Q_{AB}—B triplets. The refinement of virtual atoms on the covalent bonds between two non-H atoms resulted in deformation density peaks located in the same region as for the multipolar-atom model. The Q_{HX} virtual atoms yielded generally bonding density peaks which were not in accordance with the multipolar-atom models. Therefore, the hydrogen—Q_{HX} distances were restrained to the typical distance between the H atom and bonding density peaks appearing in the EXP_IAM Fourier residual maps. The distance H—Q_{HX} targets were 0.27, 0.34 and 0.37 Å for H—O, H—N and H—C bond charges, respectively, with a sigma restraint of 0.01 Å.

The position of oxygen electron lone pairs was stabilized by using the distance restraints d(O—Q_{LP}) = 0.28 Å and simi-

[1] Supplementary material is available from the IUCr electronic archives (Reference: PC5010). Services for accessing these data are described at the back of the journal.

larity of d(O, Q_{LP}) distances. In addition, the lone-pair positions were restrained by similarity of $A-O-Q_{LP}$ angles, where A are atoms bonded to the O atom. The similarity restraints avoid introducing specific targets which are external to the diffraction data. Planarity restraints were also applied to the lone pairs on the O=C oxygen atom belonging to the carboxylic acid.

Typical sigma values for geometry restraints were 0.01 Å for distances, 0.01 Å for similarity of distance, 0.001 Å for linearity and 0.001 for planarity (Jelsch *et al.*, 2005) restraints. In the THEO_VIR refinement, the κ values of the H atoms were also restrained to a value of 1.16 (1) (Stewart, 1976) and refined. To reduce the number of the least-squares variables and improve the convergence of the refinement, chemical equivalences were applied to the virtual and H atoms. The chemical equivalences are detected in an automatic procedure based on the chemical connectivity and geometry (Domagała *et al.*, 2011). In the case of the spherical atoms and charges model, the equivalence constraint applies to two parameters only: the P_{val} valence population and the expansion/contraction coefficient κ.

2.8. Virtual-atom theoretical refinement

The least-squares refinement *versus* theoretical structure factors was performed using all reflections up to $s = 1.25$ Å^{-1}. The refinement strategy was as follows:

(i) The starting atomic positions for all the additional charges were generated with the *MoPro* program. The bond virtual atoms were initially placed in the middle of the bonds. The oxygen lone pairs were placed at $d = 0.28$ Å from the nucleus in a trigonal geometry (LP1—O—LP2 = 120°) for the carbonyl C=O and in a tetrahedral geometry for the COH and HOH groups.

(ii) The thermal displacement parameters were all fixed to zero and the scale factor was set to unity.

(iii) The initial valence population P_{val} of all virtual charges was set to zero, which corresponds to their absence. The P_{val} population was the first parameter to be refined, enabling then the refinement of the other parameters for the virtual atoms.

(iv) Each type of parameter (P_{val}, κ, xyz) was refined successively. P_{val} and κ were refined for all atoms. The xyz positions were refined only for the virtual atoms. The procedure was cycled until convergence. The final results of the valence populations (P_{val}) and κ are presented in Table 3.

Table 3
Charge-density parameters for the THEO_VIR model.

Atom	P_{val}	κ	Atom	P_{val}	κ
Cl1	7.43 (1)	0.9900 (8)	*Q*O1C8	0.38 (1)	0.941 (9)
O1	6.17 (2)	0.943 (1)	*Q*O2C8	0.195 (8)	1.07 (2)
O2	6.26 (2)	0.967 (1)	*Q*N1C2	0.26 (1)	0.97 (1)
N1	4.25 (5)	1.033 (2)	*Q*N1H1 1, 2, 3	0.40 (1)	0.951 (7)
C1	3.34 (2)	1.046 (2)	*Q*C1C2	0.55 (1)	0.820 (7)
C2	3.21 (3)	1.036 (2)	*Q*C1C6	0.58 (1)	0.809 (6)
C3	3.17 (3)	1.029 (2)	*Q*C1C8	0.58 (1)	0.830 (6)
C4	3.04 (2)	1.032 (3)	*Q*C2C3	0.62 (1)	0.809 (6)
C5	3.10 (3)	1.037 (3)	*Q*C3C4	0.66 (1)	0.793 (6)
C6	3.07 (2)	1.030 (2)	*Q*C5C7	0.54 (2)	0.799 (8)
C7	2.78 (5)	1.048 (3)	*Q*C4C5 *Q*C5C6	0.66 (1)	0.798 (4)
C8	2.59 (3)	1.029 (4)	*Q*C4H4 *Q*C6H6	0.456 (9)	0.879 (6)
H2	0.47 (1)	1.23 (2)	*Q*C3H3	0.46 (1)	0.875 (8)
H3	0.75 (2)	1.16 (1)	*Q*C7H7 1, 2, 3	0.54 (1)	0.832 (5)
H4 H6	0.78 (1)	1.158 (7)	*Q*O2H2	0.204 (8)	1.13 (1)
H1*A* H1*B* H1*C*	0.627 (9)	1.176 (7)	*Q*OH*W* *Q*OH*W′*	0.207 (7)	1.15 (1)
H7*A* H7*B* H7*C*	0.76 (1)	1.161 (6)	LPO1 LPO1	0.169 (5)	1.44 (1)
O*W*	6.36 (2)	0.948 (1)	LPO2 LPO2′	0.092 (4)	1.55 (2)
H1*W* H2*W*	0.49 (1)	1.14 (1)	LPO*W* LPO*W′*	0.130 (5)	1.50 (2)

2.9. Transfer and refinement *versus* experimental data

The X-ray crystal structure at $s = 0.66$ Å^{-1} reciprocal resolution achieved in the laboratory for 2-carboxy-4-methylanilinium chloride monohydrate at 100 K was tested for three different charge-density transfers. In the first model, the parameters of the corresponding pseudo-atoms were transferred from the ELMAM2 database (Domagała *et al.*, 2011). Performing a multipolar refinement (THEO_MUL) and a virtual-spherical-atoms refinement (THEO_VIR) against theoretical structure factors of the title compound leads to charge-density parameters that can also be used for a transfer procedure. Hence, three alternative charge-density models (EXP_ELMAM2, EXP_MUL and EXP_VIR) were transferred to the structure of the title compound, as described in Table 2.

After charge-density transfer, the H-atom positional parameters were constrained to the neutron-determined distances of 1.083 Å for C—H, 1.033 Å for N—H and 0.967 Å for O—H (Allen *et al.*, 2004). In the EXP_VIR model transfer, the U_{ij} thermal parameters of the bond virtual atoms located between non-H atoms were constrained to take the average of the two bonded atom U_{ij} values.

The thermal parameters U_{iso} of H atoms were constrained as in the EXP_IAM refinement to ride on the U_{eq} of the carrier atom (factors 1.2 and 1.5). For virtual atoms located on H—X bonds, the U_{iso} thermal parameters were set to ride on the U_{eq} of the X-bonded atom, with intermediate multiplying coefficients of 1.1 for the H—C atoms on the aromatic ring and 1.3 for the others.

The lone-pair (LP) atoms had their U_{ij} parameters set equal to that of the carrying O atom. Finally, for the three transfers, the scale factor, the position and thermal U_{ij} parameters of the heavy atoms (C, O, N, Cl) were refined together until convergence.

3. Results and discussion

3.1. Crystal structure

The molecular structure with thermal ellipsoids is shown in Fig. 1. The carboxylic acid is slightly tilted with respect to the aromatic ring by an angle of 14.7 (1)°. The Cl^- anion forms three salt bridges involving the three different H atoms of the NH_3^+ groups of neighbouring organic cations $(HOOC–C_7H_6–NH_3)^+$ (Table 4). In addition, the Cl^- anion interacts with one water H atom and more weakly with three H—C groups. The crystal cohesion is also ensured by two O—H···O and one N—H···O hydrogen bonds and two weak C—H···O hydrogen bonds.

Table 4
Geometry of the hydrogen bonds and salt bridges in the EXP_ELMAM2 model.

D—H···A	D—H (Å)	H···A (Å)	D···A (Å)	D—H···A (°)
O2—H2···OW^{i}	0.981	1.706	2.660 (3)	163.4
N1—H1A···O1^{ii}	1.033	2.414	2.726 (3)	96.2
C6—H6···O2^{ii}	1.083	2.374	2.730 (3)	97.2
OW—H1···OW^{iii}	0.956	1.971	2.915 (2)	168.7
C7—H7C···O2^{vi}	1.059	2.571	3.523 (3)	149.4
OW—H2W···Cl^{ii}	0.967	2.141	3.107 (3)	176.9
N1—H1C···Cl^{ii}	1.033	2.086	3.115 (3)	173.7
N1—H1B···Cl^{iv}	1.033	2.169	3.199 (2)	174.4
N1—H1A···Cl^{v}	1.033	2.287	3.289 (5)	162.8

Symmetry codes: (i) $-x, y+\frac{1}{2}, -z+\frac{1}{2}$; (ii) x, y, z; (iii) $-x-1, y+\frac{1}{2}, -z+\frac{1}{2}$; (iv) $x, y-1, z$; (v) $-x, -y-1/2, -z+1/2$; (vi) $-x, -y+1, -z+1$.

Table 5
Statistics for the crystallographic refinements *versus* the experimental and theoretical structure factors for the different atom models.

The Fourier residual $\Delta\rho$ maps (e Å^{-3}) were computed using the reflections up to a resolution of d = 0.7 Å. GOF = goodness of fit.

	EXP				THEO		
Model	IAM	ELMAM2	MUL	VIR	IAM	MUL	VIR
No. of variables	118	118	118	118	0	248	76 + 26
$R(F)$ (%)	3.9	3.3	3.31	3.45	1.53	0.67	0.65
wR^2 (I) (%)	14.6	12.9	12.3	13.0	5.20	0.92	1.60
GOF (I)	1.24	1.04	1.04	1.10			
$\Delta\rho_{max}$	0.43	0.25	0.31	0.32	0.71	0.073	0.144
$\Delta\rho_{min}$	−0.29	−0.25	−0.35	−0.36	−0.32	−0.16	−0.182
r.m.s.($\Delta\rho$)	0.067	0.058	0.059	0.061	0.080	0.0098	0.019

Fig. 3 shows the projection of the molecular crystal structure packing of CMA along the **b** direction. The molecular packing can be described as alternating organic–inorganic chains in which the organic cations, chloride anions and water molecules are connected by a three-dimensional network of hydrogen bonds. One can distinguish six types of hydrogen bonds: O—H···Cl$^-$, N—H···Cl$^-$, C—H···Cl$^-$, O—H···O, C—H···O and N—H···O. The distances and angles describing the hydrogen bonds are summarized in Table 4. Each organic molecule is involved in five different intermolecular interactions. The organic cations are linked together only *via* one strong hydrogen bond from the ammonium group towards the carboxylic group (N1—H1A···O1) to form zigzag chains along the a axis.

The water molecule plays an important role in the molecular packing. Each water molecule interacts with a symmetry-related water molecule through the OW—H1W···OW hydrogen bond to form a chain parallel to the c axis. In addition, the water molecule acts as a hydrogen-bond donor to the Cl$^-$ anion and an acceptor to the COH group in the carboxylic acid.

There is a weak C—H···O-type hydrogen bond between the oxygen O2 atom of the COH group and H7C of the methyl moiety. The weak C6—H6···O2 hydrogen bond is intramolecular and generates a five-membered cycle.

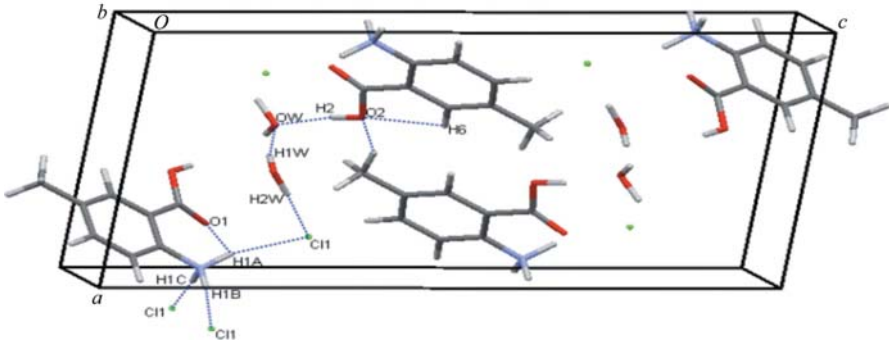

Figure 3
Molecular packing of CMA along the b axis showing the hydrogen-bond interactions. Hydrogen bonds are drawn as dashed lines.

In order to further examine the intermolecular contacts in CMA, a Hirshfeld surface analysis was performed with *CrystalExplorer* (Spackman & McKinnon, 2002; McKinnon *et al.*, 2004, 2007). It has been shown recently that tools based on Hirshfeld surfaces are a very efficient method for quantifying intermolecular interactions in molecular crystals. It was based on the EXP_ELMAM2 molecular structure and aimed to determine the nature of the intermolecular contacts in the crystal packing. The highest fraction in the CMA crystal is H···H contacts (40.0%). Other contributions are in decreasing order: O···H (24.6%), Cl···H (16.1%), C···H (14.1%), C···C (2.6%), C···O (1.7%) and O···Cl (0.9%). The hydrogen bonds represent therefore as much as 40.6% of the surface contacts.

3.2. Quality of the charge-density models

The statistics for the different refinements of X-ray diffraction data are listed in Table 5. The four models refined against experimental data represent different charge-density distributions. The number of restraints and variables refined is the same for the four models. As expected, when compared to the standard EXP_IAM spherical-atom model, the three models that take into account the deformation of the molecular electron density show improved crystallographic statistics. The two multipolar-atom models, however, show lower R factors than the real + virtual spherical charges model. This can be explained, in part, by the greater flexibility of the multipolar-atom model for which the number of parameters (Table 5) describing the charge density is more than doubled compared to the virtual-atoms model (Table 2).

The quality of the charge-density models was also assessed by analysing the Fourier residual electron-density maps. The residual maps are shown in Fig. 4 in the aromatic plane of CMA. The EXP_IAM model shows the characteristic non-modelled bonding deformation density remaining in the residual map. The residual density, however, is weaker in the lone-pair

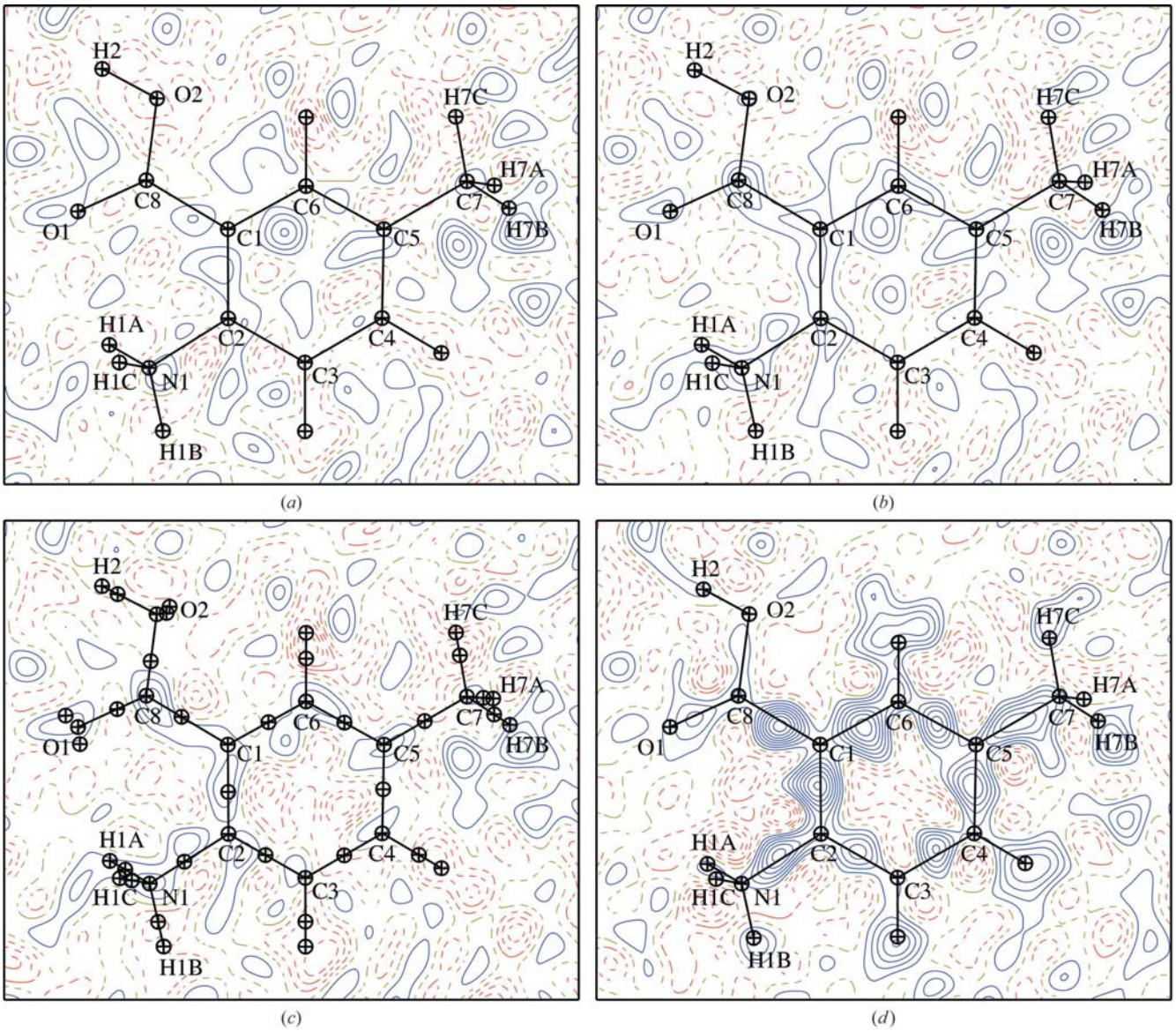

Figure 4
Experimental residual electron density in the aromatic plane of 2-carboxy-4-methylanilinium chloride monohydrate: (*a*) ELMAM2, (*b*) MUL, (*c*) VIR and (*d*) IAM models. Contour level: ± 0.05 e Å^{-3}. Blue solid lines and red dashed lines denote positive and negative contours, respectively. The zero contour is shown as a yellow line.

regions (see the supplementary material) as these are more contracted in real space than the bonding density and therefore require higher resolution to be refined and displayed in Fourier maps. (The O atoms in Fig. 4 are slightly out of plane, which further attenuates the lone-pair residual density.)

An accurate electron-density modelling should result in a fit of the diffraction data good enough to ensure that only random noise appears in the residual maps. This is the case for the three models taking into account the deformation density. The electron lone-pair regions do not show significant residual density for the EXP_VIR model (see the supplementary material). The root-mean-square (r.m.s.) of the experimental residual electron density is reduced by 13% for the multipolar models compared to EXP_IAM. For the EXP_VIR model, the decrease is only 9% (Table 5), although the bonding density features have disappeared. The EXP_ELMAM2 and EXP_MUL representations achieve a slightly better electron-density modelling than EXP_VIR. The number of parameters describing the charge density is much higher with the EXP_MUL multipolar model compared to EXP_VIR, which may explain the lower *R* factors of the former model. The number of charge-density parameters is also reduced in the ELMAM2 databank transfer as local symmetries are applied to the multipoles; therefore many small parameters are set to zero. For the theoretical residual densities, the reduction (by a factor of 4 and 8) is drastic for the multipolar and virtual modelling, respectively.

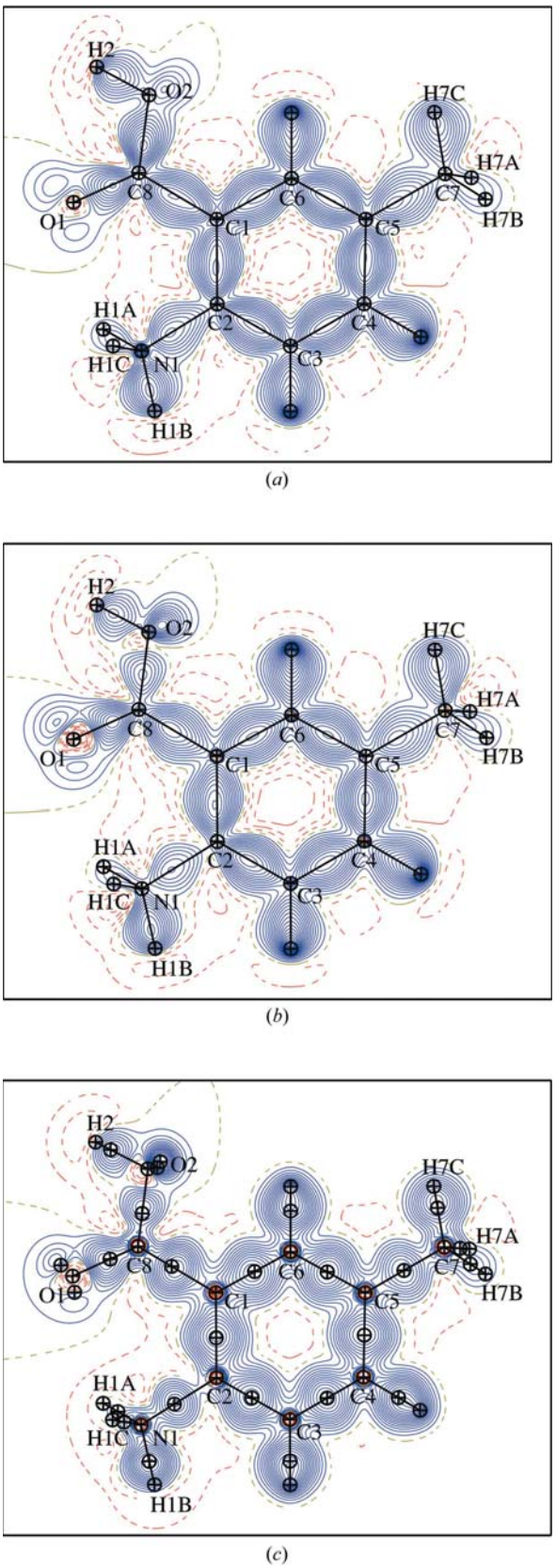

Figure 5
Static deformation electron density in the aromatic plane of the title compound: (*a*) EXP_ELMAM2, (*b*) EXP_MUL and (*c*) EXP_VIR models. Contours as in Fig. 4.

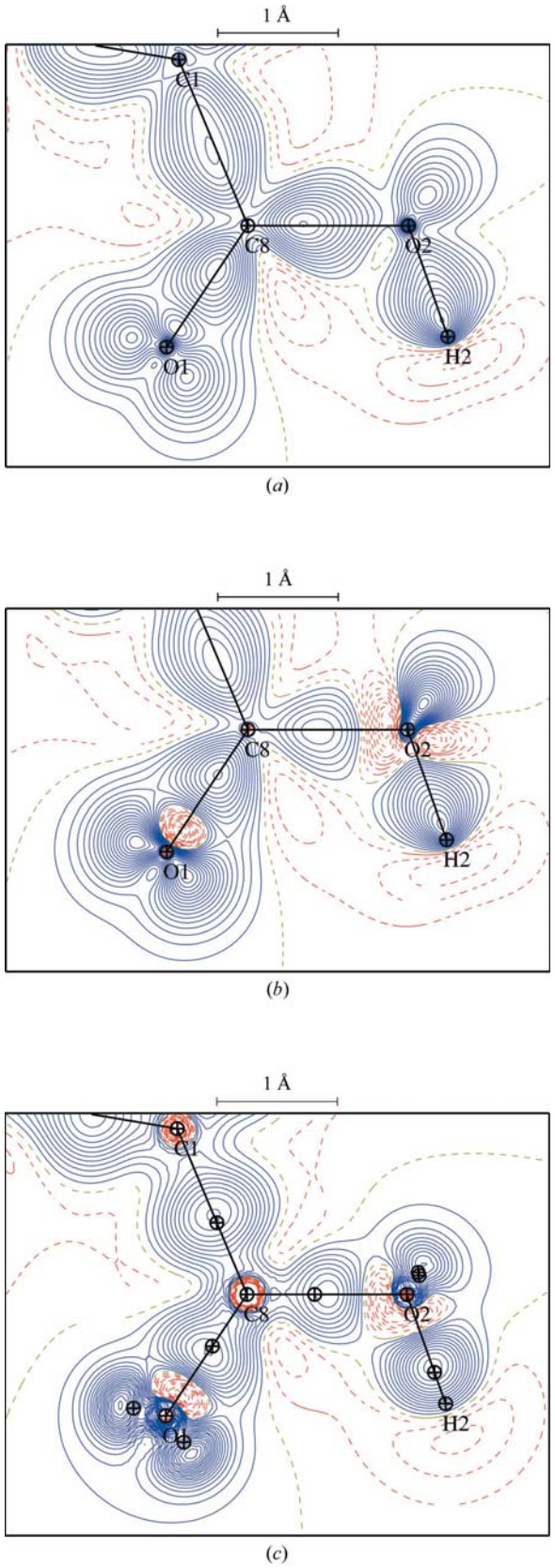

Figure 6
Static deformation electron density in the plane of the COO group: (*a*) EXP_ELMAM2, (*b*) EXP_MUL and (*c*) EXP_VIR models. Contours as in Fig. 4.

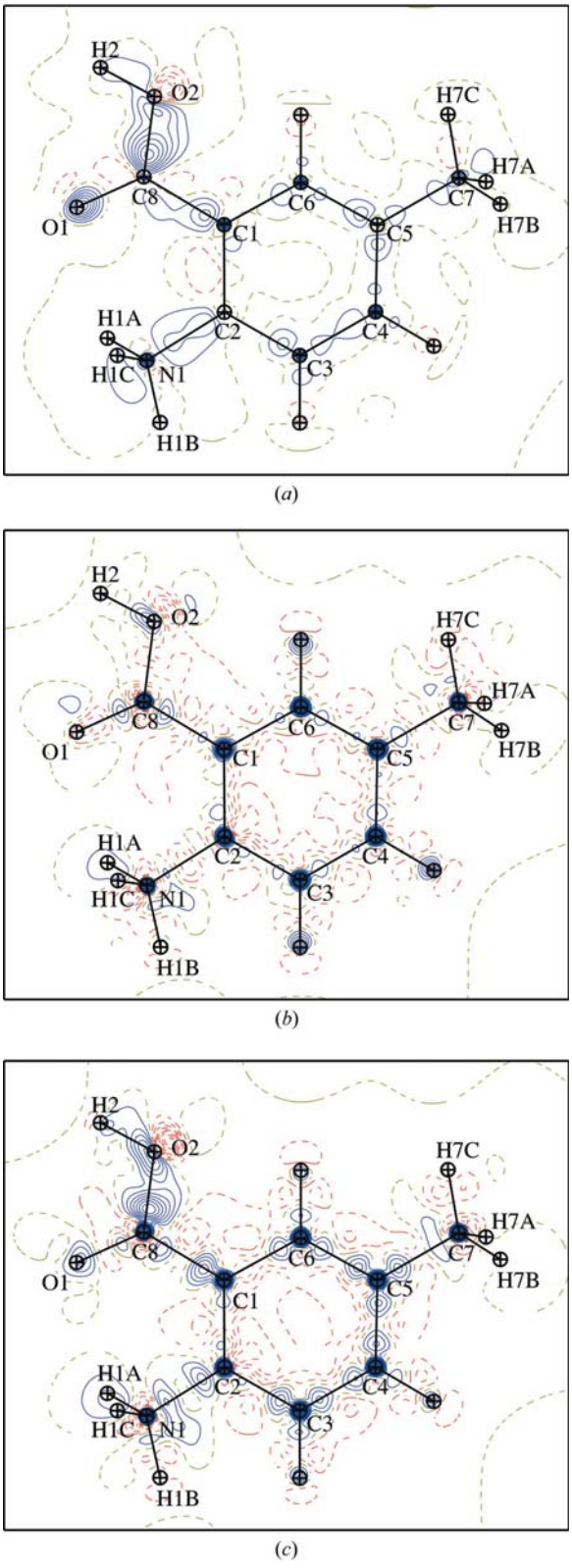

Figure 7
Difference between models of static deformation electron density shown in the aromatic plane. (*a*) ELMAM2_MUL, (*b*) MUL_VIR and (*c*) ELMAM2_VIR. Contour level: ± 0.02 e Å^{-3}. Blue solid lines and red dashed lines denote positive and negative contours, respectively. The zero contour is shown as a yellow line.

Table 6
Correlation coefficient between the deformation electron densities ρ_{def} calculated in the asymmetric unit from the three charge-density models (the r.m.s. value is given in the last line).

Correlation	EXP_ELMAM2	EXP_MUL	EXP_VIR
EXP_MUL	0.933		
EXP_VIR	0.903	0.928	
ρ_{def}(r.m.s.)	0.0797	0.0811	0.0837

3.3. Deformation electron densities

The deformation electron density is defined as the difference between the total molecular density described by the multipolar-atom or dummy-bond-charge model and the superposition of spherical independent atoms (IAM). Deformation maps of the static electron density in the aromatic plane and in the sp^2 plane of carboxylic acid (containing the lone pairs of atom O1) are shown in Figs. 5 and 6.

The difference between the deformation electron-density maps (see Fig. 7) indicates the dissimilarities between the models. The largest discrepancy is found around the carboxylic acid C atom between ELMAM2 and the two other models. The same maps were computed with only atom C8 contributing and they show the same discrepancy. This suggests that the C atom of the carboxylic acid may be poorly modelled in the ELMAM2 database.

The difference maps are qualitatively in accordance with the computed correlation coefficients. The EXP_ELMAM2 and EXP_MUL maps agree qualitatively well (Table 6) and display the highest correlation coefficient r = 0.93. The correlation between the EXP_VIR and the EXP_MUL models is nearly as high. The lowest correlation is found between EXP_ELMAM2 and EXP_VIR, but still reaches 90%.

The EXP_VIR map shows systematically high negative deformation electron-density peaks in the close vicinity of the atomic nuclei. The bonding electron density is generally of similar height in EXP_VIR compared to the multipolar models. On the other hand, the electron lone pairs show the strongest deformation density in the EXP_VIR maps. However, the main observation concerning electron lone pairs is the lower level reached for the ELMAM2 map, as the database is derived from experimental results.

Globally, the three charge-density models show the same r.m.s. magnitude (within ±3%) of deformation density (Table 6).

For all three models, the bonding electron-density peaks are centred on the C—C atomic bonds, while for the C—N bond the electron density is closer to the N atom, which is more electron withdrawing. The refined distances $d(Q, \mathrm{C})$ = 0.819 (2) Å and $d(Q, \mathrm{N})$ = 0.647 (1) Å in the EXP_VIR model give a clear picture of the N—C bond dissymmetry.

The C—C bonds of the benzene ring show deformation peak heights ranging from 0.55 to 0.60 e Å^{-3} for the EXP_ELMAM2 and EXP_MUL models, and about 0.60 e Å^{-3} for the EXP_VIR model.

One major discrepancy between the multipolar and virtual spherical-atom models is the absence of visible electron depletion near the H atoms H—C in the latter case. The more electron-depleted H atom bonded to the O atom does, however, show a deficit of electrons in all three maps of Fig. 6. The deformation density peaks on the C—H bonds appear to be closer to the H atoms and the maxima amount to 0.85, 0.90 and 0.75 e Å^{-3} for the ELMAM2, MUL and VIR models, respectively.

The electron lone-pair geometry on the three O atoms, which are of different chemical type, can be compared in the VIR model with respect to the Q_{LP1}—O—Q_{LP2} angle. The angle value is 131° in the water molecule, which is larger than the 109.5° angle of the tetrahedral geometry. In the C—O—H oxygen atom of the carboxylic acid, the angle is 96°, which is lower than the tetrahedral 109.5° angle and can be related to resonance effects with the neighbouring sp^2 atoms of the C═O atoms. The electron lone pairs of the hydroxy group tend to be closer to each other when the neighbouring C atom is aromatic or of sp^2 hybridization (Zarychta *et al.*, 2007). In the carboxylic acid, the angle Q_{LP1}—O—Q_{LP2} is 137° for the C═O group and is larger than the 120° angle of the trigonal geometry. The peak heights on the carbonyl lone pairs are 0.60, 0.85 and 0.90 e Å^{-3} for the ELMAM2, MUL and VIR models, respectively (Fig. 6).

3.4. Electrostatic potential

The software *VMoPro* allows calculation of the electrostatic properties from the charge-density description of a molecule. This property is an invaluable tool for understanding molecular interactions. The electrostatic potential (ESP) generated by the organic cation alone was computed and the 0.001 e Å^{-3} electron-density surface is coloured according to the ESP value in Fig. 8. The ESP is mostly positive around the cation and shows a qualitatively similar colour value for all three models around the different types of chemical functional groups. The lowest ESP value is found near the two O atoms of the carboxylic acid, while the NH_3^+ moiety and (secondarily) CH_3 groups show the highest ESP.

In all three models, the positive electrostatic potential is very large compared to the negative potential, which is confined near two O atoms. The negative potential around the carbonyl O atom is strongest in the EXP_VIR model compared to the two multipolar models.

To compare the models quantitatively, the ESP was computed in a volume around the van der Waals surface of the CMA molecule (Fig. 1), at a distance ranging from 0 to 2 Å. The maximum, minimum and r.m.s. values of the ESP are presented in Table 7 and are quantitatively similar between the three models within ±15%.

A good quantitative agreement is observed between the r.m.s. ESP values for the three models; the EXP_ELMAM2 ESP shows a slightly higher r.m.s. value compared to EXP_MUL. On the other hand, the EXP_VIR model shows a 10% attenuated ESP.

Table 7
Correlation coefficient of the electrostatic potential *V* calculated from the three electron-density models applied on the experimental crystal structure.

The statistics on *V* (e Å^{-1}) are computed in a volume from *d* = 0 to 2 Å outside the van der Waals surface of 2-carboxy-4-methylanilinium chloride monohydrate.

Correlation	EXP_ELMAM2	EXP_MUL	EXP_VIR
EXP_MUL	0.978		
EXP_VIR	0.922	0.962	
V(max)	0.208	0.240	0.279
V(min)	−0.196	−0.189	−0.180
V(r.m.s.)	0.061	0.053	0.051

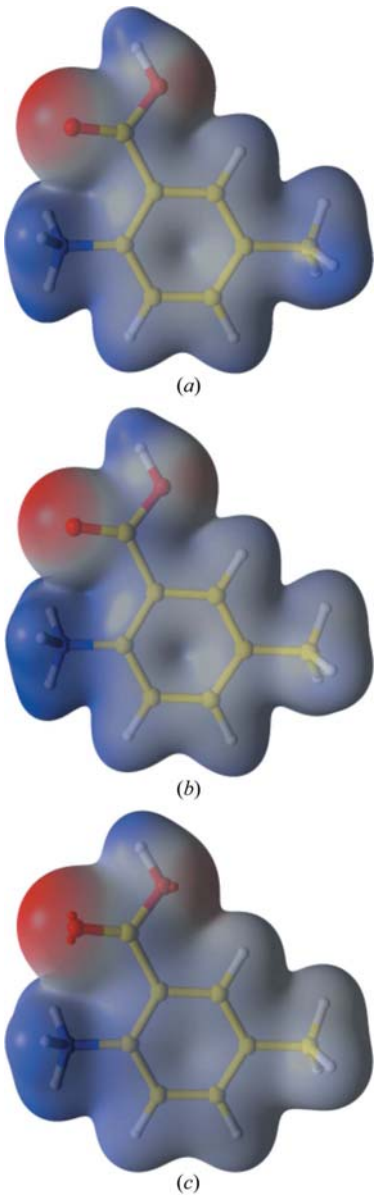

Figure 8
Electrostatic potential of the electron density generated by the organic cation molecule on the 0.01 e Å^{-3} isosurface: (*a*) EXP_ELMAM2, (*b*) EXP_MUL and (*c*) EXP_VIR models. The maximum negative (red) and positive (blue) values of the ESP correspond to −0.001 and 0.3 e Å^{-1} values. The view was generated with the *MoProViewer* program (Guillot, 2011).

The correlation coefficients between the electrostatic potential arising from the three different charge-density models are also listed in Table 7. The two models refined *versus* the theoretical data (EXP_VIR and EXP_MUL) display a very high correlation (r = 0.962). For the two mostly unrelated models, EXP_VIR and EXP_ELMAM2, the correlation still reaches r = 0.922.

The dipole moment of the CMA compound is represented in Fig. 9. The dipole moments derived from the EXP_ELMAM2, EXP_MUL and EXP_VIR models have magnitudes of 12.4, 10.3 and 8.7 D, respectively. The dipole moment is dominated by the positions and charges of the chloride anion and ammonium group, as they generate a dipole of 7.9 D alone, for the MUL model. The MUL and VIR dipole moments have similar directions as the angle between the two vectors is 8°. The ELMAM2 dipole moment shows more discrepancy both in magnitude and direction with the MUL and VIR models, as the angles are 17 and 25°, respectively.

3.5. H—*X* distances

The effect of the different charge-density models transferred on the H—*X* distances in the experimental structure of the title compound was analysed. The different structures were complemented by the additional refinement of the H-atom coordinates without any H—*X* distance constraint/restraint application. Fig. 10 shows the resulting average distance of the various types of H—*X* bonds and the standard values obtained from neutron diffraction (Allen *et al.*, 2004). As expected, the H—*X* distances from the IAM spherical-atom model are generally lower by about 0.1 Å than the neutron distances. The distances obtained from the optimization are systematically slightly larger (by 0.013 Å on average) than the neutron distances.

The N—H and C—H (methyl) distances show a very good consistency within the three transferred charge-density models and are in accordance with the standard neutron-diffraction distances. The C(sp^2)—H bonds within the benzoic acid ring show a lower but still good consistency.

The ELMAM2 modelling leads to larger than expected OH distances for the three O—H groups. The O2—H2···O*W* hydrogen bond is quite strong ($d_{H\cdots O}$ = 1.971 Å, Table 4); therefore the O2—H2 distance is expected to be lengthened (Steiner & Saenger, 1994) with respect to the standard neutron distance (d_{OH} = 0.967 Å). The O2—H2 and O*W*—H1*W* donor groups are involved in a unique O—H···O-type hydrogen bond with an O—H···O angle larger than 160°; therefore the formula proposed by Yukhnevich (2009), which links the distances d_{OH} and $d_{O\cdots H}$, can be applied. The distance d_{O2-H2} = 0.981 Å computed this way indeed turns out to be higher than the neutron-diffraction distance (Fig. 10). For this H atom, all three charge-density models yield a significantly higher O2—H2 distance. For the weaker hydrogen bond O*W*—H1*W*···O*W* between water molecules, the calculated distance is shortened and is in best agreement with the EXP_VIR model. The lower agreement for the O—H distances between neutron (or calculated values) and the three charge-density models can be attributed to the intrinsic higher thermal motion of this type of H atom (Madsen, 2006) which is even worse on the more agitated water molecule (Fig. 1).

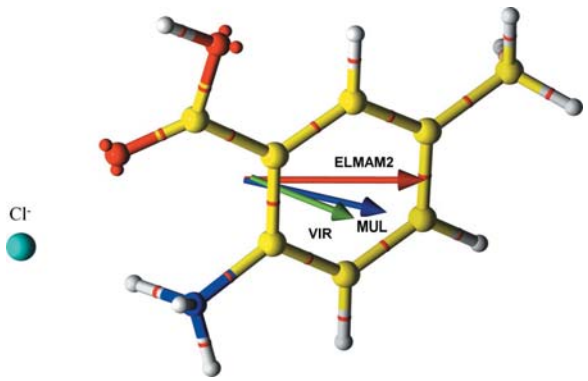

Figure 9
Dipole moment of the CMA compound represented for the three charge-density models. The origin is at the centre of mass.

4. Conclusion

The current study of the new crystal structure of 2-carboxy-4-methylanilinium chloride monohydrate determined from X-ray diffraction data realistically demonstrates that the extended ELMAM2 database transfer approach greatly improves several factors, such as hydrogen atomic positions and residual electron densities, when these are compared with the corresponding EXP_IAM model.

The structure was analysed in terms of its geometry, molecular packing and intra- and intermolecular interactions. The Hirshfeld surface analysis of intermolecular contacts showed that the H···H followed by O···H are the dominating contacts in this crystal structure.

In this study on the CMA structure, in the absence of high-resolution diffraction data, the ELMAM2 databank was applied to estimate the charge density. This electron density is

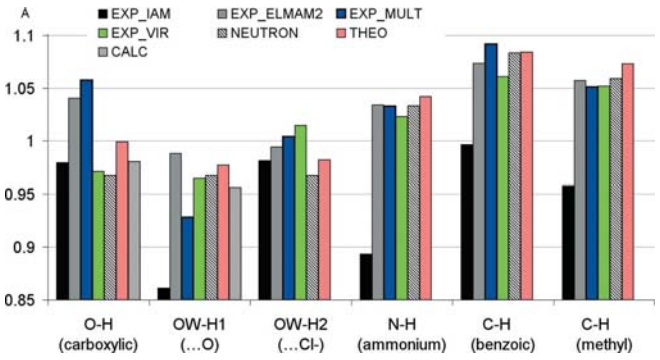

Figure 10
H—*X* distances occurring in the refined crystal structure with the different models. The ammonium N—H, methyl and aromatic C—H distances are averaged. The standard distances from neutron diffraction (Allen *et al.*, 2004) are also shown. For the carboxyl O···H and water O*W*—H1 bonds, involved in an O—H···O hydrogen bond, the distance was calculated by the Yukhnevich (2009) method.

comparable to that obtained by refinement *versus* theoretical structure factors using the multipolar-atom model and the spherical atoms plus charges model. The crystallographic refinement statistics (Table 5) are improved and the residual maps are clearer with all the three charge-density models compared to the spherical-atom refinement. The spherical atoms plus charges model, however, has fewer parameters to model the electron density and the crystallographic statistics are intermediate between the two multipolar models and the IAM method.

A structural refinement with no H—*X* distance constraints reproduces generally the H—*X* bond lengths expected from the neutron-diffraction formula much better for the three electron-density models than for the EXP_IAM model. The proper modelling of the electron density reduces the bias on atomic positions. A high-order diffraction data collection is still necessary for a charge-density refinement of a molecule in its crystal environment.

The electrostatic potential distributions around the CMA cation and around the whole asymmetric unit were calculated. All three electron-density models display highly correlated ESPs. The electrostatic interaction energies with dimers in the crystal estimated from three models agree and correlate well. The THEO_VIR model shows, however, an attenuation in the r.m.s. magnitude of the ESP and electrostatic energies. A current limitation of the bond virtual-atoms model is its inability to model the ellipticity of the bonding density in aromatic rings and around sp^2-type atoms. This could be achieved by defining elliptical κ expansion/contraction coefficients and could further improve the quality of the electron-density and electrostatics modelling.

N. Dadda is grateful for a fellowship from the University of Khenchela.

References

Afonine, P. V., Grosse-Kunstleve, R. W., Adams, P. D., Lunin, V. Y. & Urzhumtsev, A. (2007). *Acta Cryst.* D**63**, 1194–1197.

Afonine, P. V., Lunin, V. Y., Muzet, N. & Urzhumtsev, A. (2004). *Acta Cryst.* D**60**, 260–274.

Allen, F. H., Watson, D. G., Brammer, L., Orpen, A. G. & Taylor, R. (2004). *International Tables for Crystallography*, Vol. C, ch. 9.5, pp. 790–811. Heidelberg: Springer.

Bąk, J. M., Dominiak, P. M., Wilson, C. C. & Woźniak, K. (2009). *Acta Cryst.* A**65**, 490–500.

Blessing, R. H. (1997). *J. Appl. Cryst.* **30**, 421–426.

Brock, C. P., Dunitz, J. D. & Hirshfeld, F. L. (1991). *Acta Cryst.* B**47**, 789–797.

Cao, S. L., Feng, Y.-P., Jiang, Y.-Y., Liu, S. Y., Ding, G. Y. & Li, R. T. (2005). *Bioorg. Med. Chem. Lett.* **15**, 1915–1917.

Cao, S. L., Feng, Y. P., Zheng, X. L., Jiang, Y. Y., Zhang, M., Wang, Y. & Xu, M. (2006). *Archiv Pharm.* **339**, 250–254.

Cao, S. L., Guo, Y. W., Wang, X. B., Zhang, M., Feng, Y. P. Jiang, Y. Y., Wang, Y., Gao, Q. & Ren, J. (2009). *Archiv Pharm.* **342**, 182–189.

Clementi, E. & Roetti, C. (1974). *At. Data Nucl. Data Tables*, **14**, 177–478.

Coppens, P., Abramov, Y., Carducci, M., Korjov, B., Novozhilova, I., Alhambra, C. & Pressprich, M. R. J. (1999). *J. Am. Chem. Soc.* **121**, 2585–2593.

Dietrich, H., Scheringer, C., Meyer, H., Schulte, K.-W. & Schweig, A. (1979). *Acta Cryst.* B**35**, 1191–1197.

Dittrich, B., Hübschle, C. B., Holstein, J. J. & Fabbiani, F. P. A. (2009). *J. Appl. Cryst.* **42**, 1110–1121.

Dittrich, B., Hübschle, C. B., Luger, P. & Spackman, M. A. (2006). *Acta Cryst.* D**62**, 1325–1335.

Dittrich, B., Hübschle, C. B., Messerschmidt, M., Kalinowski, R., Girnt, D. & Luger, P. (2005). *Acta Cryst.* A**61**, 314–320.

Dittrich, B., McKinnon, J. J. & Warren, J. E. (2008). *Acta Cryst.* B**64**, 750–759.

Dittrich, B., Munshi, P. & Spackman, M. A. (2007). *Acta Cryst.* B**63**, 505–509.

Dittrich, B., Strumpel, M., Schäfer, M., Spackman, M. A. & Koritsánszky, T. (2006). *Acta Cryst.* A**62**, 217–223.

Dittrich, B., Weber, M., Kalinowski, R., Grabowsky, S., Hübschle, C. B. & Luger, P. (2009). *Acta Cryst.* B**65**, 749–756.

Domagała, S. & Jelsch, C. (2008). *J. Appl. Cryst.* **41**, 1140–1149.

Domagała, S., Munshi, P., Ahmed, M., Guillot, B. & Jelsch, C. (2011). *Acta Cryst.* B**67**, 63–78.

Dovesi, R., Saunders, V. R., Roetti, C., Orlando, R., Zocovich-Wilson, C. M., Pascale, F., Civalleri, B., Doll, K., Harrison, N. M., Bush, I. J., D'Arco, Ph. & Llunell, M. (2010). *CRYSTAL-09 User's Manual*. University of Turin, Turin, Italy.

Guillot, B. (2011). *Acta Cryst.* A**67**, C511–C512.

Guillot, B., Viry, L., Guillot, R., Lecomte, C. & Jelsch, C. (2001). *J. Appl. Cryst.* **34**, 214–223.

Hansen, N. K. & Coppens, P. (1978). *Acta Cryst.* A**34**, 909–921.

Hariharan, P. C. & Pople, J. A. (1973). *Theor. Chim. Acta*, **28**, 213–222.

Hirshfeld, F. L. (1971). *Acta Cryst.* B**27**, 769–781.

Hohenberg, P. & Kohn, W. (1964). *Phys. Rev. B*, **136**, 864–871.

Jelsch, C., Guillot, B., Lagoutte, A. & Lecomte, C. (2005). *J. Appl. Cryst.* **38**, 38–54.

Jelsch, C., Pichon-Pesme, V., Lecomte, C. & Aubry, A. (1998). *Acta Cryst.* D**54**, 1306–1318.

Lee, C., Yang, W. & Parr, R. G. (1988). *Phys. Rev. B*, **37**, 785–789.

McKinnon, J. J., Jayatilaka, D. & Spackman, M. A. (2007). *Chem. Commun.* pp. 3814–3816.

McKinnon, J. J., Spackman, M. A. & Mitchell, A. S. (2004). *Acta Cryst.* B**60**, 627–668.

Madsen, A. Ø. (2006). *J. Appl. Cryst.* **39**, 757–758.

Mullen, D. & Hellner, E. (1977). *Acta Cryst.* B**33**, 3816–3822.

Mullen, D. & Hellner, E. (1978*a*). *Acta Cryst.* B**34**, 1624–1627.

Mullen, D. & Hellner, E. (1978*b*). *Acta Cryst.* B**34**, 2789–2794.

Pichon-Pesme, V., Jelsch, C., Guillot, B. & Lecomte, C. (2004). *Acta Cryst.* A**60**, 204–208.

Pichon-Pesme, V., Lecomte, C. & Lachekar, H. (1995). *J. Phys. Chem.* **99**, 6242–6250.

Scheringer, C. (1980). *Acta Cryst.* A**36**, 205–210.

Scheringer, C., Kutoglu, A., Mullen, D. & Hellner, E. (1978). *Acta Cryst.* A**34**, 475–476.

Scheringer, C., Mullen, D. & Hellner, E. (1978). *Acta Cryst.* A**34**, 621–625.

Scheringer, C., Mullen, D., Hellner, E., Hase, H. L., Schulte, K.-W. & Schweig, A. (1978). *Acta Cryst.* B**34**, 2241–2243.

Sheldrick, G. M. (2008). *Acta Cryst.* A**64**, 112–122.

Spackman, M. A. & McKinnon, J. J. (2002). *CrystEngComm*, **4**, 378–392.

Steiner, T. & Saenger, W. (1994). *Acta Cryst.* B**50**, 348–357.

Stewart, R. F. (1976). *Acta Cryst.* A**32**, 565–574.

Volkov, A., Li, X., Koritsanszky, T. & Coppens, P. (2004). *J. Phys. Chem. A*, **108**, 4283–4300.

Yukhnevich, G. V. (2009). *Crystallogr. Rep.* **54**, 184–189.

Zarychta, B., Pichon-Pesme, V., Guillot, B., Lecomte, C. & Jelsch, C. (2007). *Acta Cryst.* A**63**, 108–125.

Zheng, B. H., Fang, Z. J., Jiao, Y., Jiang, Y. H. (2007). *Jiangsu Chem. Ind.* **1**, pp. 39–41, 55. doi: CNKI:ISSN:1002-1116.0.2007-01-015